Ice-confined synthesis of highly ionized 3D-quasilayered polyamide nanofiltration membranes

Ice-confined Synthesis of Highly Ionized 3D-quasi-layered Polyamide Nanofiltration Membranes

Yanqiu Zhang[1,2], Hao Wang[1], Jing Guo[1], Xiquan Cheng[3], Gang Han[4], Cher Hon Lau[5], Haiqing Lin[6], Shaomin Liu[7], Jun Ma[2], Lu Shao[1]*

Affiliations:

[1] MIIT Key Laboratory of Critical Materials Technology for New Energy Conversion and Storage, State Key Laboratory of Urban Water Resource and Environment (SKLUWRE), School of Chemistry and Chemical Engineering, Harbin Institute of Technology, Harbin 150001, China

[2] School of Environment, Harbin Institute of Technology, Harbin 150009, China

[3] School of Marine Science and Technology, Sino-European Membrane Technology Research Institute, Harbin Institute of Technology, Weihai 264209, China

[4] College of Environmental Science and Engineering, Nankai University, 38 Tongyan Road, Jinnan District, Tianjin 300350, China

[5] School of Engineering, The University of Edinburgh, King's Buildings, Mayfield Road, Edinburgh EH9 3JL, UK

[6] Department of Chemical and Biological Engineering, University at Buffalo, The State University of New York, Buffalo, NY, 14260, USA

[7]WA School of Mines: Minerals, Energy and Chemical Engineering, Curtin University Perth, WA (Australia)

*Correspondence to: shaolu@hit.edu.cn

Abstract: Existing polyamide (PA) membrane synthesis protocols are underpinned by controlling diffusion-dominant liquid-phase reactions that yield sub-par spatial architectures and ionization behavior. We report an ice-confined interfacial polymerization strategy to enable the effective kinetic control of the interfacial reaction and thermodynamic manipulation of the hexagonal polytype (I_h) ice phase containing monomers to rationally synthesize 3D-quasi-layered PA membrane for nanofiltration. Experiments and molecular simulations confirmed the underlying membrane formation mechanism. Our ice-confined PA nanofiltration membrane featured high-density ionized structure and exceptional transport channels, realizing superior water permeance and excellent ion-selectivity.

One-Sentence Summary: Ice-confined Interfacial Polymerization Membrane for Nanofiltration

Main Text: Introduction: Membrane-based separation technologies, characterized by high energy efficiency, low carbon emissions, and high design flexibility, have evolved into an effective-sustainable approach for alleviating global water scarcity, environmental remediation and resource recovery (*1-4*). Nanofiltration (NF) has emerged as a cost-effective membrane separation process for efficiently rejecting small molecules and multivalent ions, showing immense promise in wastewater treatment, water softening and purification processes (*5*).

Polyamide (PA) membranes prepared via interfacial polymerization (IP) are the benchmark NF membranes (*6, 7*). The nanostructures and ionization behavior of PA membranes have been identified to play a crucial role in determining the membrane separation performance (i.e., permeability and selectivity). Since the rate of polycondensation reactions between organic amines and acyl chlorides is several orders of magnitude faster than the diffusion rate of the amines in the organic phase solution during IP, the ideal PA NF membrane architectures are hard to achieve by conventional diffusion-dominant IP (*5*). Researchers have attempted to control the temperature of the organic phase and the m-phenylenediamine (MPD) soaked substrate to adjust the transmission rate of diamine during IP (*8-11*), however, the current diffusion-dominant monomer distribution lacks spatial regulation, resulting in insufficient membrane crosslinking or growth inhibition. Other molecular engineering approaches have been proposed by tailoring the chemical structures of the monomers, incorporating nanomaterials with charges onto the membrane surface and interior, and utilizing reactive monomers with ionizable groups to obtain high low-/high-valent ion selectivity (*12*).

Ice chemistry engineering is a promising approach for producing composite materials with 3D hierarchical or anisotropic architectures, such as nacre-like ceramics (*13*), cellular polymeric composites (*14*), hydrogels and aerogels (*15, 16*). The ice-melting process can elegantly manipulate the molecular packing behavior during crystalline synthesis, and the solid-liquid phase transition significantly changes the reaction kinetics and thermodynamics of material synthesis (*17, 18*). The dissolved reactants in ice can be controllably released due to the confined effect of the ice I_h phase (*19*). Herein, we conceived an ice-confined interfacial polymerization (IC-IP) strategy to synthesize highly ionized 3D-quasi-layered PA NF membrane by utilizing an ice-melting-induced ice/water phase transition. This phase transition process can deliberately control the diffusion and reaction rates of the MPD monomers in the I_h "ice" phase as the confined interface.

IC-IP synthesis was conducted at the interface between the MPD-ice (**Fig. 1A-1B and Fig. S1-S2)** and n-hexane solution (freezing point of approximately –95.3 °C) containing trimesoyl chloride (TMC). The MPD aqueous solution was frozen at –20 °C. Subsequently, the TMC/n-hexane solution (pre-cooled to ambient temperature) was added to the MPD-ice surface. As the frozen MPD-ice slowly melted, MPD was gradually released. In contrast to the conventional PA NF (C-PANF) membrane formed at the water/n-hexane interfaces with a dense heterogeneous structure **(Fig. 1C and Fig. S3-S4**), the unique 3D-quasi-layered wrinkled architecture (**Fig. 1D-E and Fig. S5-S6**) for ice-confined PA NF (IC-PANF) membrane can be created via ice chemistry engineering.

Structure characterizations of IC-PANF membranes

Scanning electron microscopy (SEM) and atomic force microscopy (AFM) measurements demonstrated that the IC-PANF membrane with a regular wrinkled structure was relatively rougher than the C-PANF membrane (**Fig. 1D and Fig. S6**), resulting in a two-fold increase in the accessible surface area of the IC-PANF membrane (**Table S1 and Fig. S7**). Furthermore, the IC-PANF membrane maintained a dominant fraction of sub-nanometer pores (**Fig. S8**), indicating that the IC-PANF membrane possessed a larger water-accessible surface area for faster water transport and well-defined selective pores. Transmission electron microscopy (TEM) revealed that the IC-PANF membrane consisted of a packed, interconnected microporous layered internal structure (**Fig. 1E**), and positron annihilation spectroscopy (PAS) measurements elucidated that the substitution of the MPD-aqueous solution with MPD-ice resulted in a significant increase in the fractional internal free volume of the PA layer (**Fig. S9**). To further probe the internal structure, the 3D-void-microstructure was reconstructed using focused ion beam-scanning electron microscopy (FIB-SEM), confirming that the IC-PANF membrane comprised larger microvoid stacks of 3D-quasi layers (**Fig. S10**), which was consistent with the TEM and PAS results. In contrast, the C-PANF membrane was mostly dense with no observable microscale pores or layers (**Fig. 1C**). The simultaneous increase in surface wrinkles and interior microporosity was unique to IC-PANF membrane obtained *via* ice chemistry engineering.

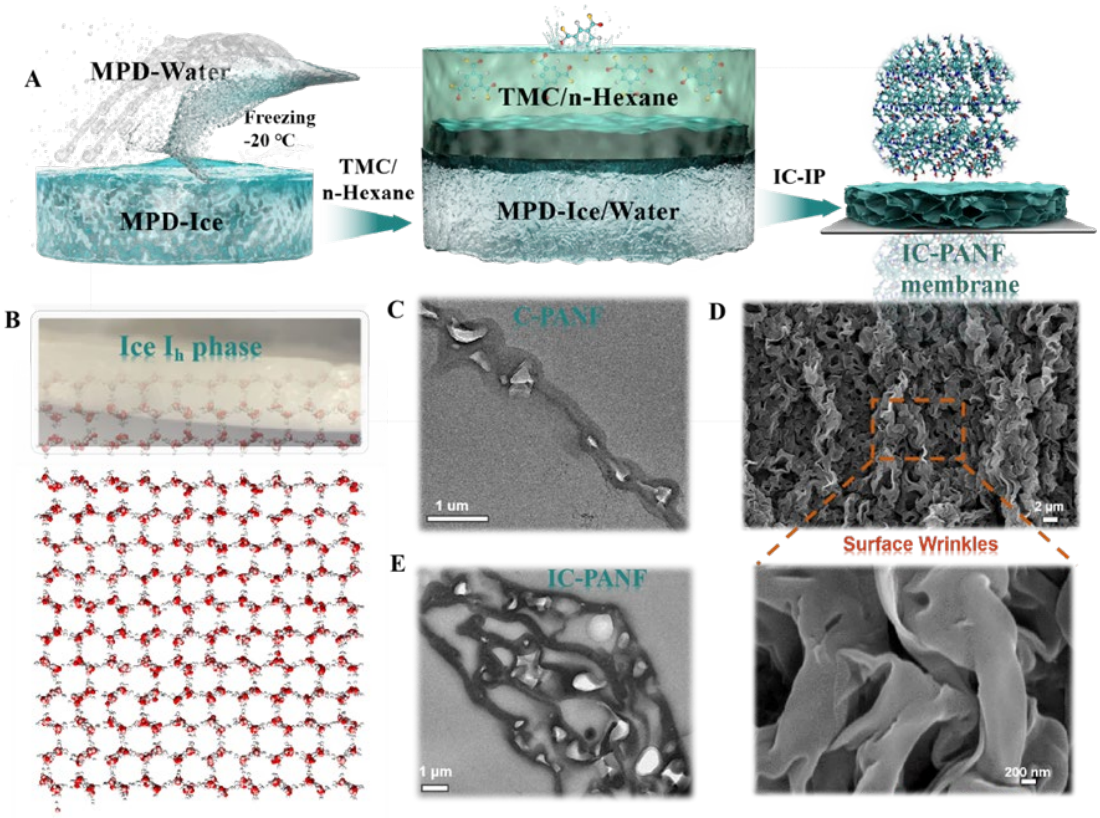

Fig. 1. Ice-confined interfacial polymerization and PA NF membrane structure. (A) Schematic of the IC-IP at the ice/n-hexane interface; (B) Ice I_h phase; TEM cross-sectional images of the (C) C-PANF and (E) IC-PANF membranes; (D) SEM images of the IC-PANF membrane surface under different magnifications.

Mechanism of IC-IP

To elucidate the synergistic effects of the diffusion kinetics and ice-melting thermodynamics on the spatial architecture of the PA membrane during synthesis, the molecular mechanisms and process characteristic timescales were investigated. Ice melting is the least hindered phase transition, requiring the disruption of the crystalline order to achieve the liquid phase. With the stepwise increase in temperature, the molecular diffusion rate in ice is gradually accelerated. Upon reaching the melting point (T_m), the ice began to melt and transition into a solid/liquid phase (**Fig. 2A**). Therefore, the formation of the IC-PANF membrane during IC-IP synthesis can be interpreted by breaking down the MPD-ice phase temperature ($T_{MPD\text{-}p}$) into four stages: i) $T_{MPD\text{-}p} < T_m$, ii) $T_{MPD\text{-}p} = T_m$, iii) $T_{MPD\text{-}p} > T_m$, and iv) $T_{MPD\text{-}p} = T_a$ (ambient temperature) (**Fig. S11**).

Compared to bulk water, the higher viscosity of a quasi-liquid layer and lower potential energy of ice are crucial for developing a large-area wetting layer (*17, 20*). Molecular dynamics (MD) simulations revealed that TMC molecules tended to anchor on the MPD-ice surface (ice-like liquid water layer) when reaching equilibrium at the first stage ($T_{MPD\text{-}p} < T_m$, in **Fig. S12-S16**) (*21*). With an increase in the MPD concentration in ice, more TMC molecules were anchored on the ice surface, and a high adsorption energy ($|E_{ads}|$) was achieved by hydrogen bonding and van der Waals forces (**Fig. 2B**). This regulated the build-up of MPD and TMC in a planar two-dimensional space was conducive to their polymerization in a constricted interfacial liquid layer (**Fig. S12-16 and**

Table S2). In contrast, TMC and MPD reacted rapidly in a traditional IP process, making it difficult to control the distribution of TMC at the interface. At $T_{MPD\text{-}p}=T_m$, ice began to melt and formed an ice/water-hexane interface. At this point, the diffusion kinetics and reaction thermodynamics of TMC and MPD were vital for PA membrane formation at the ice/water-hexane interface (*22*). MD simulations **in Fig. 2C** revealed that the MPD diffused slower at the ice/water-hexane interface when equilibrium reached at T_m. This was mainly attributed to the confinement of MPD molecules within the ice, where the absolute value of the binding free energy between ice and MPD ($\Delta G_{binding(MPD\text{-}ice)}$= –34.9 kcal mol^{-1}), was significantly higher than the MPD with water ($\Delta G_{binding(MPD\text{-}water)}$= –14.6 kcal mol^{-1}) (**Fig. 2A**), and the adsorption of TMC on the ice surface (at $T_{MPD\text{-}p} < T_m$) synergized with the high viscosity of the MPD-ice/water mixture (**Fig. S17**). In particular, the confinement effect of ice also impacted the MPD concentration in the ice/water phase. This can be further manifested by tracking the release kinetics of MPD monomers from ice. As the ice started to melt, the MPD concentration initially showed a rapid increase and then decreased during the ice-melting process (**Fig. S18**). The larger MPD concentration gradient and lower MPD diffusion rate led to the formation of a loose heterogeneous macroporous structure at $T_{MPD\text{-}p} = T_m$ (**Fig. S19A**). When $T_{MPD\text{-}p}$ was higher than T_m, all ice crystals melted into water, and the MPD phase temperature increased from T_m to T_a. At this stage, the reaction rate between MPD and TMC decreased, as demonstrated by a reduction in the Gibbs free energy (ΔG from –38.6 to –42.8 kJ mol^{-1}) (**Fig. 2D**). MPD reacted with TMC through the gaps/channels of the previously formed macroporous layer to create new layers via IP (*11*). During the melting process, gases dissolved in the ice were released, which was also conducive to the formation of an internal microporous-layered structure (**Fig. S11**) (*11, 23, 24*). The SEM results and separation performance of the IC-PANF membrane as a function of temperature during IC-IP were consistent with the above analysis (**Fig. S19 and S20**). As a result, this underpinned the formation of a 3D-quasi-layered architecture under the coupling effects of controlled monomer diffusion kinetics and ice-melting engineered thermodynamics during IC-IP synthesis.

The inherent structures of MPD-ice nucleation and the IC-PANF membrane strongly depended on the MPD concentration (*23, 24*). Variations in T_m and enthalpy (ΔH_m) with ice melting were monitored by differential scanning calorimetry **(Fig. S21 and S22)**, where the T_m of MPD-ice decreased from –0.2 to –3.0 °C, and the ΔH_m of ice reduced from 359.4 to 87.9 J g^{-1} as the initial MPD concentration increased. The decrease in the number of H-bonded water molecules with MPD at high concentrations suppressed ice nucleation. This hindered the freezing of water (**Fig. S23-S27**) and prevented water molecules from forming ordered hydrogen-bond networks, which was the geometrical basis for crystallization and lowered T_m and ΔH_m *(25)*. These changes altered the MPD concentration and diffusion rate at the interface during IC-IP synthesis for unique membrane structure formation (**Fig. S18 and S28-S29**).

The freezing duration was also an essential parameter in tailoring the nucleation and crystallization of MPD-ice, which could disrupt the distribution and release of MPD from ice. I_h-ice crystals were obtained after 8 h of freezing, yielding 3D-quasi-layered architectures (**Fig. 2E and Fig. S30-S33**). Shorter freezing times (0.5 h, 2 h) were insufficient to crystallize the MPD-water into ice. Furthermore, a longer freezing time (12 h) resulted in an undesirable pore structure due to the partial precipitation and accumulation of MPD molecules on the ice surface by MPD solute segregation (*26*). Moreover, T_a had a noticeable effect on the IC-IP process **(Fig. S34 and S35)**. Lower T_a reduced the melting rate of MPD-ice and the release of MPD. Simultaneously, owing to the high viscosity and high surface tension of organic solvents at low temperature, the dissolution of MPD was reduced, leading to the formation of defects on the PA membrane surface. At a higher

T_a, the melting rate of ice was accelerated during the IC-IP process and the ice-confining role was inevitably weakened, resulting in the formation of a dense PA layer with lower water permeance. The optimal T_a to yield 3D-quasi-layered PA membranes was 28 °C, which is similar to the temperature deployed in incumbent processes and those used in industry.

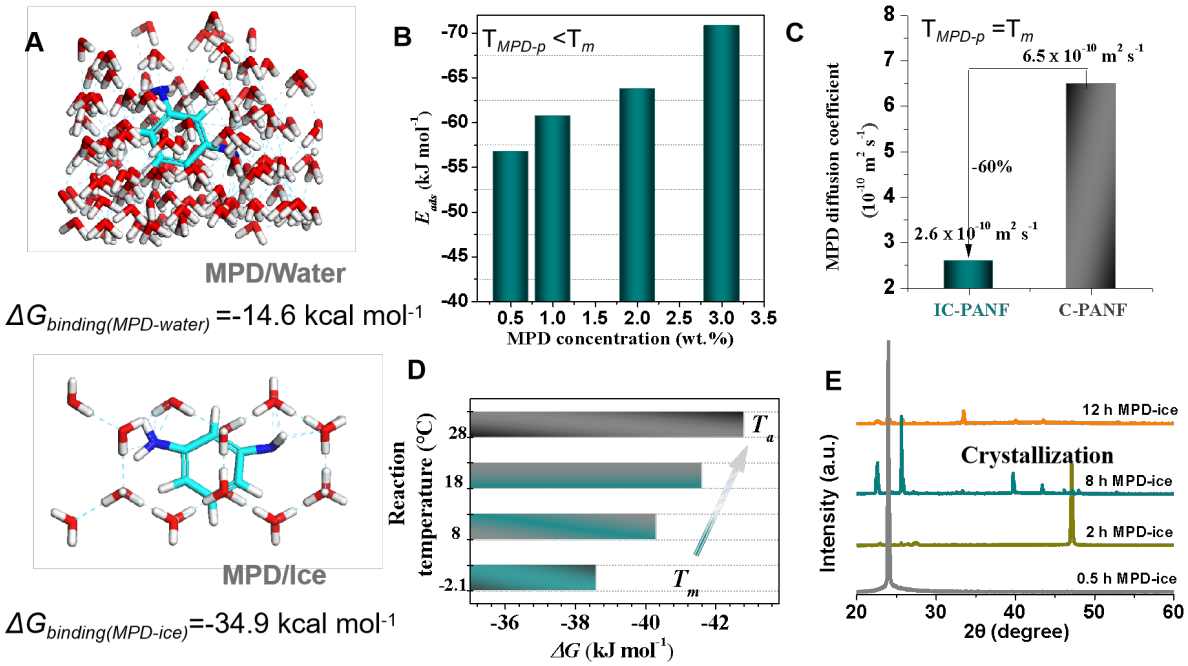

Fig. 2. Mechanism of IC-IP. (A) Schematic of the structural evolutions of MPD-ice and MPD-water and the Gibbs binding free energy ($\Delta G_{binding}$) at $T_{MPD\text{-}p}=T_m$ by MD simulation; (B) The E_{ads} of TMC with varying concentrations of MPD-ice at the n-hexane/ice interface; (C) MD simulations of the MPD diffusion coefficient at the initial reaction temperature for conventional IP (28°C) and IC-IP (-2.1 °C); (D) ΔG for the MPD interaction with TMC from T_m to T_a by density functional theory (DFT); (E) XRD results of MPD-ice at different freezing times.

Membrane ionization behavior

The 3D-quasi-layered structure endowed the IC-PANF membrane with a high ionization density, which was crucial for enhancing the separation efficiency of charged species in aqueous solutions. Bulk water is a favorable medium for R-COOH ionization, in which the highly polarizable water molecules can readily stabilize the electrostatic charge of R-COO^-. R-COOH intensively located on the membrane surface and in large inherent pores (>>2 nm) satisfied the ionizing conditions (*27*). The quantitative ion chromatography results verified that the associated areal R-COO^- densities significantly increased for the IC-PANF membrane compared to the C-PANF membrane (**Fig. 3A, B**). The abundant -COOH (as noted in the XPS results) on the surface and interior of the IC-PANF membrane (**Fig. S36-S38 and Table S3-S6**) and the 3D interconnected layered network with internal larger microvoids significantly amplified the exposed water-contacted surface, promoting the ionization of R-COOH (**Fig. 3A, B**). Meanwhile, the areal R-NH_3^+ densities of the IC-PANF membrane illustrated single-pKa (pKa~9.5) ionization of R-NH_3^+ and high areal R-NH_3^+ densities **(Fig. 3C).** Therefore, the IC-PANF membrane obtained via ice chemistry engineering remained highly ionized over a wide pH range. The ionization behavior of the IC-PANF membrane can be interpreted by the ionization of R-COOH and R-NH_2 at different pH (**Fig. 3D and S39**): 1) pH<5, 2) pH=5 to 9.5, and 3) pH>9.5 At the first stage with pH<5, all the R-NH_2 was converted

to R-NH_3^+, and there was no change in its ionization. As the solution pH approached 5, ionization of surface R-COOH gradually occurred. When entering the second stage (from pH 5 to 9.5), the surface R-COOH was fully ionized, while the interior R-COOH was subsequently ionized. In the final stage (pH>9.5), R-NH_3^+ was completely deprotonated (all were R-NH_2). Thus, the zeta potential of the IC-PANF membrane was lower than that of the C-PANF membrane when the pH>5. The salt separation efficacy of the synthesized membranes as a function of the pH was preliminarily assessed using a Na_2SO_4 solution (**Fig. 3E**). At pH<5, SO_4^{2-} was rejected due to Na^+ exclusion by R-NH_3^+ to maintain solution electroneutrality. As the pH increased to 5, the Na_2SO_4 rejection reached a minimum value owing to surface R-COOH ionization. The diminished SO_4^{2-} rejection at this point likely stemmed from the increased salt sorption. SO_4^{2-} rejection increased substantially until pH>5 for the IC-PANF membrane, where the deprotonation of R-NH_3^+ and interior R-COOH significantly enhanced SO_4^{2-} exclusion.

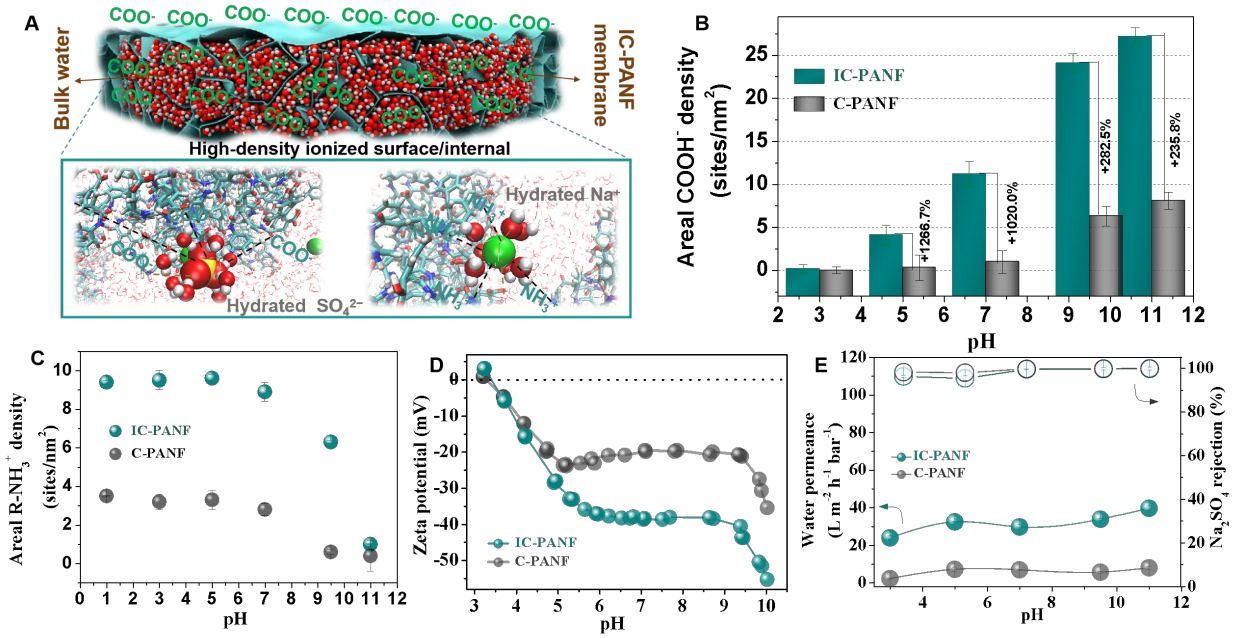

Fig. 3. Ionization behavior of IC-PANF and C-PANF membranes. (A) Schematic of the highly ionization behavior of the IC-PANF membrane segment (the 3D interconnected layered network with internal larger microvoids amplified the exposed water-contacted surface) and a snapshot of the diffusion of H_2O, Na^+ and SO_4^{2-} inside the pores (green spheres for Na^+ and yellow spheres for SO_4^{2-} by molecular simulation); (B, C) Areal R-COO^- and R-NH_3^+ density as a function of pH by experiments; (D) Zeta potential, (E) water permeance and Na_2SO_4 rejection as a function of pH. Error bars represent the standard deviations of three independent measurements.

Membrane ion-sieving performance

We further evaluated the membrane separation performance using various salts tests to explore the structure-ionization-property relationships. Compared with the C-PANF membrane, the IC-PANF membrane exhibited a ~four-fold enhancement in water permeance (i.e., from 6.8 to 29.7 L m^{-2} h^{-1} bar^{-1}) with an unnoticeable reduction in Na_2SO_4 rejection. We also compared the performance with other state of the art PA NF membranes **(Fig. 4A and Table S7)** (*7, 28-38*). The enlarged interconnected 3D-quasi-layered and highly ionization features endowed the IC-PANF membrane with excellent hydrophilicity and high-water adsorption ability, resulting in fast water pathways

with low resistance (**Fig. S40-S41 and Table S8**). The salt rejection of the IC-PANF membrane decreased in the order of Na_2SO_4 (99.6%) > $MgSO_4$ (93.2%) > $MgCl_2$ (78.3%) > NaCl (42.5%) (**Fig. 4B**). The separation mechanism of the IC-PANF membrane for various salts was dominated by the synergistic effect of Donnan repulsion, size sieving and dielectric exclusion. The higher ionization R-COOH groups endowed the membrane with highly negatively charged densities on the surface and interior; therefore, the Donnan repulsion for SO_4^{2-} was stronger than that for Cl^-. In addition, the ion solvation energy barrier (when ions transfer from the bulk solution to the membrane pores with low permittivity) and the hydration radius of Cl^- are smaller than that of SO_4^{2-} (**Table S9**) (*27, 39*). As a result, the IC-PANF membrane possessed a higher rejection to SO_4^{2-} than Cl^- and exhibited a single NaCl/Na_2SO_4 selectivity of up to 143.8 (**Fig. S42 and Table S10**).

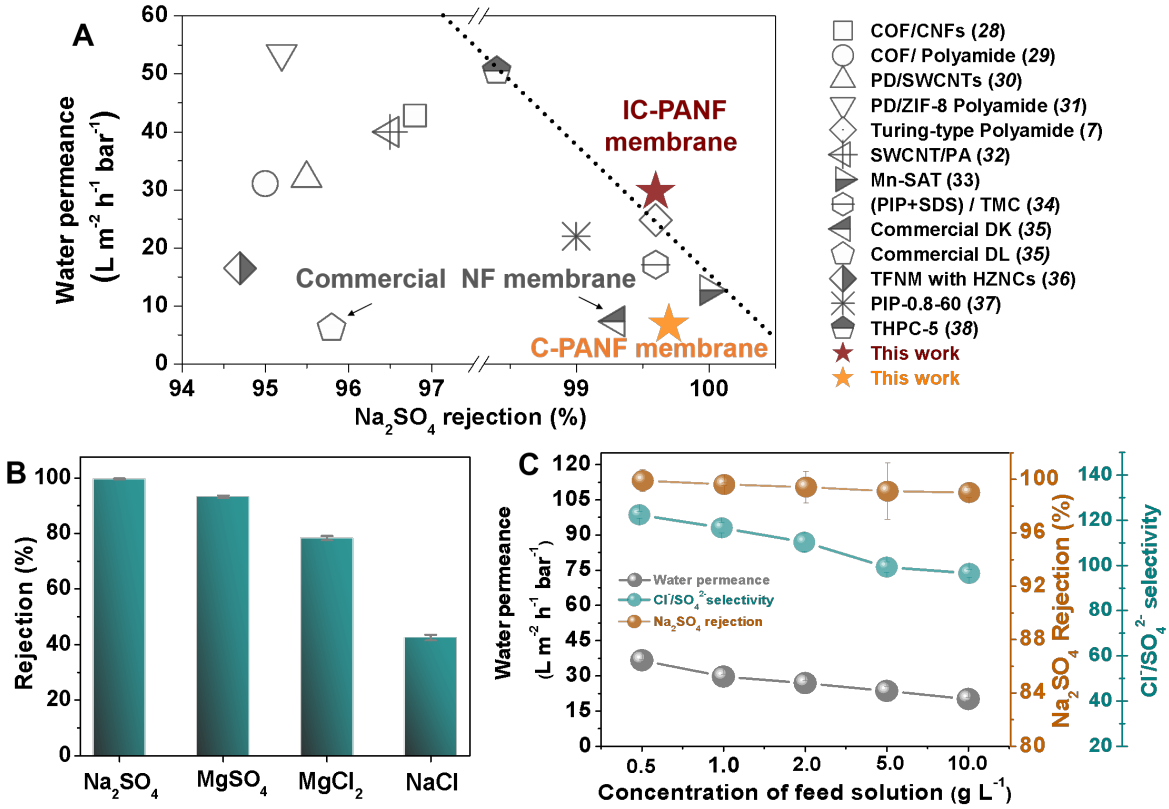

Fig. 4. Salt separation performance and ion selectivity of the IC-PANF membrane. (A) Performance comparison of the IC-PANF membrane with other state of the art membranes for separating Na_2SO_4. The red star represents the as-prepared IC-PANF membrane (Table S7); (B) The separation performance of IC-PANF membrane for various salts; (C) The water permeance, Na_2SO_4 rejection and the co-ion Cl^-/SO_4^{2-} selectivity of IC-PANF membrane with varying feed concentrations. Error bars represent the standard deviations of three independent measurements.

Given that real saline water consists of a mixture of inorganic salts, we further measured the co-ion Cl^-/SO_4^{2-} selectivity using a mixture of NaCl and Na_2SO_4. Cl^-/SO_4^{2-} separation is beneficial for recovering valuable salt resources and obtaining clean freshwater (*5*). The substitution of the MPD aqueous solution with MPD-ice achieved a six~ten-fold higher co-ion Cl^-/SO_4^{2-} selectivity in the IC-PANF membrane compared with the C-PANF membrane (**Fig. 4C and Fig. S43**). When

increasing the feed solution concentration, the electrostatic screening effects were enhanced, which reduced the membrane charge density and weakened the electrostatic repulsion for ions, resulting in a decline in the Cl^-/SO_4^{2-} selectivity or salt rejection. However, owing to the lower sensitivity to the charge densities of the highly ionization structures, the IC-PANF membrane retained a higher Cl^-/SO_4^{2-} selectivity and Na_2SO_4 rejection even at high salt concentrations (**Fig. 4C and Fig. S43**). The IC-PANF membrane also demonstrated excellent ion-sieving for different co-ion systems, superior long-term separation performance, and promising antifouling properties (**Fig. S44-S48**). This co-ion selectivity provides promise for brine refinement and salt reclamation. Most importantly, our ice-confined synthesis strategy can be extended to diverse IP processes **(Fig. S49-S50)**.

In summary, we developed an IC-IP method to engineer the spatial architectures and ionization behavior of PA NF membrane. The synergetic control of the reaction kinetics and thermodynamics of ice-melting during IC-IP led to the formation of a highly ionized 3D-quasi-layered structure that combined high water permeance and unparalleled co-ion sieving abilities. We foresee that with the help of the presented strategy, a versatile "ice-confined" synthesis approach can enrich the current chemistry toolbox for synthesizing membranes and diverse advanced materials.

References and Notes

1. S. Li *et al*., *Science* **377**, 1555-1561 (2022).
2. T. E. Culp *et al*., *Science* **371**, 72-75 (2021).
3. M. R. Chowdhury, J. Steffes, B. D. Huey, J. R. McCutcheon, *Science* **361**, 682-686 (2018).
4. H. B. Park, J. Kamcev, L. M. Robeson, M. Elimelech, B. D. Freeman, *Science* **356**, eaab0530 (2017).
5. C. Zhao *et al*., *Nat. Commun.* **14**, 1112 (2023).
6. R. Dai *et al*., *Nat Water*, **1**, 281–290 (2023)
7. Z. Tan, S. Chen, X. Peng, L. Zhang, C. Gao, *Science* **360**, 518-521 (2018).
8. A. K. Ghosh, B. H. Jeong, X. Huang, E. M. V. Hoek, *J. Membr. Sci.* **311**, 34-45 (2008).
9. B. Khorshidi, T. Thundat, B. A. Fleck, M. Sadrzadeh, *Sci. Rep* **6**, 22069 (2016).
10. Q. Zhao, D. L. Zhao, T. S. Chung, *Adv. Funct. Mater.* **7**, 1902108 (2020).
11. X.H. Ma *et al*., *Environ. Sci. Technol. Lett.* **5**, 123-130 (2018).
12. Y. Yang *et al*., *Science* **364**, 1057-1062 (2019).
13. C. Huang *et al*., *Angew. Chem. Int. Ed.* **58**, 7636-7640 (2019).
14. J. Han *et al*., *Adv. Funct. Mater.* **29**, 1900412 (2019).
15. J. Zhou *et al*., *Adv. Mater.* **34**, 2106897(2022,).
16. M. Hua *et al*., *Nature* **590**, 594-599 (2021).
17. B. Slater, A. Michaelides, *Nat. Rev. Chem* **3**, 172-188 (2019).
18. E. B. Moore, V. Molinero, *Nature* **479**, 506-508 (2011).
19. H. Wei *et al*., *Angew. Chem. Int. Ed.* **57**, 3354-3359 (2018).
20. H. Li *et al*., *Angew. Chem. Int. Ed.* **60**, 7697-7702 (2021).
21. M. A. Sánchez *et al*., *Proc. Natl. Acad. Sci. U.S.A.* **114**, 227-232 (2017).
22. C. Liu *et al*., *Angew. Chem. Int. Ed* **60**, 14636-14643 (2021).
23. L. E. Peng *et al*., *ACS EST Eng.* **2**, 903-912 (2022).
24. K. Grzebyk, M. D. Armstrong, O. Coronell, *J. Membr. Sci.* **644**, 120112 (2022).
25. Q. Zhang *et al*., *Nat. Commun.* **11**, 4463 (2020).

26. Z. Guo *et al*., *Angew. Chem. Int. Ed* **58**, 12569-12573 (2019).
27. C. L. Ritt *et al*., *Proc. Natl. Acad. Sci. U.S.A.* **117**, 30191-30200 (2020).
28. H. Yang *et al*., *Nat. Commun.* **10**, 2101 (2019).
29. Z. Zhang, X. Shi, R. Wang, A. Xiao, Y. Wang, *Chem. Sci.* **10**, 9077-9083 (2019).
30. Y. Zhu *et al*., *Small* **12**, 5034-5041 (2016).
31. Z. Wang *et al*., *Nat. Commun.* **9**, 2004 (2018).
32. S. Gao et al., *ACS Nano* **13**, 5278-5290 (2019).
33. J. Wang *et al*., *Nat. Commun.* **11**, 3540 (2020).
34. Y. Liang *et al*., *Nat. Commun.* **11**, 2015 (2020).
35. H. Saidani, N. B. Amar, J. Palmeri, A. Deratani, *Langmuir* **26**, 2574-2583 (2010).
36. Z. Sun *et al*., *Nano Lett.* **19**, 2953-2959 (2019).
37. Y. Liu *et al*., *Environ. Sci. Technol.* **54**, 1946-1954 (2020).
38. H. Peng *et al*., *Adv. Mater.* **332**, 2001383 (2020).
39. N. Fridman-Bishop, K. A. Tankus, V. Freger, *J. Membr. Sci.* **548**, 449-458 (2018).
40. G. Hurwitz, G. R. Guillen, E. M. V. Hoek, *J. Membr. Sci.* **349**, 349-357 (2010).
41. A. S. Michaels, *Sep. Sci. Technol.* **15**, 1305-1322 (1980).
42. J. A. Otero *et al*., *J. Membr. Sci.* **309**, 17-27 (2008).
43. Y. Li *et al*., *J. Membr. Sci.* **476**, 10-19 (2015).
44. B. Li *et al*., *Nat. Commun.* **11**, 1198 (2020).
45. Z. Ali *et al*., *Adv. Mater.* **32**, 2001132 (2020).
46. A. Hudait *et al*., *J Am Chem Soc* **140**, 4905-4912 (2018).
47. X. Liu *et al*., *J. Mater. Chem. A* **8**, 23555-23562 (2020).
48. Y. Qiu *et al*., *J Am Chem Soc* **141**, 7439-7452 (2019).
49. Z. Zhou *et al*., *ACS Nano* **15**, 11970-11980 (2021).
50. J. P. Perdew *et al*., *Phys Rev Lett 7* **77**, 3865-3868 (1996).
51. B. Delley, *J. Chem. Phys.* **113**, 7756-7764 (2000).
52. B. Delley, *J. Chem. Phys.* **92**, 508-517 (1990).
53. Z. Jiang *et al*., *Proc. Natl. Acad. Sci. U.S.A.* **117**, 30191-30200 (2020).
54. B. Yuan *et al*., *ACS Appl. Mater. Interfaces* **10**, 43057-43067 (2018).
55. Y. Hao *et al*., *J. Mater. Chem. A* **8**, 5275-5283 (2020).
56. K. Shen, P. Li, T. Zhang, X. Wang, *J. Membr. Sci.* **607**, 118153 (2020).
57. Z. M. Zhan *et al*., *J. Membr. Sci.* **604**, 118067 (2020).
58. Y. Zhang *et al*., *Sci Adv* **7**, eabe8706(2021).
59. W. Fang, L. Shi, R. Wang, *J. Membr. Sci.* **468**, 52-61 (2014).
60. P. Sarkar, S. Modak, S. Karan, *Adv. Funct. Mater. 3* **31**, 2007054 (2021).

Acknowledgments: We thank Dr. Sui Zhang from the National University of Singapore for PAS tests.

Funding: This work was supported by the National Natural Science Foundation of China (22178076, 22208072 and 21905067), the Natural Science Foundation of Heilongjiang Province for Distinguished Young Scholars (JQ2020B001), Heilongjiang Touyan Team (HITTY-20190033), China Postdoctoral Science Foundation (2021M690829), Special support from China Postdoctoral Science Foundation (2021TQ0088), Open Project of State Key Laboratory of Urban Water Resource and Environment (Harbin Institute of Technology; No. QA202127) and Royal Society (UK, IECNSFC201329).

Author contributions: Y.Z., L.S. conceived the concept. L.S. supervised the project. Y. Z. performed the experiments and characterizations. All authors wrote the manuscript and contributed to the analysis and discussion of the data.

Competing interests: The authors declare no competing interests.

Data and materials availability: All data are available in the main text or the supplementary materials.

Fig. 1. Ice-confined interfacial polymerization and PA NF membrane structure. (A) Schematic of the IC-IP at the ice/n-hexane interface; (B) Ice I_h phase; TEM cross-sectional images of the (C) C-PANF and (E) IC-PANF membranes; (D) SEM images of the IC-PANF membrane surface under different magnifications.

Fig. 2. Mechanism of IC-IP. (A) Schematic of the structural evolutions of MPD-ice and MPD-water and the Gibbs binding free energy ($\Delta G_{binding}$) at $T_{MPD\text{-}p}=T_m$ by MD simulation; (B) The E_{ads} of TMC with varying concentrations of MPD-ice at the n-hexane/ice interface; (C) MD simulations of the MPD diffusion coefficient at the initial reaction temperature for conventional IP (28°C) and IC-IP (-2.1 °C); (D) ΔG for the MPD interaction with TMC from T_m to T_a by density functional theory (DFT); (E) XRD results of MPD-ice at different freezing times.

Fig. 3. Ionization behavior of IC-PANF and C-PANF membranes. (A) Schematic of the highly ionization behavior of the IC-PANF membrane segment (the 3D interconnected layered network with internal larger microvoids amplified the exposed water-contacted surface) and a snapshot of the diffusion of H_2O, Na^+ and SO_4^{2-} inside the pores (green spheres for Na^+ and yellow spheres for SO_4^{2-} by molecular simulation); (B, C) Areal R-COO^- and R-NH_3^+ density as a function of pH by experiments; (D) Zeta potential, (E) water permeance and Na_2SO_4 rejection as a function of pH. Error bars represent the standard deviations of three independent measurements.

Fig. 4. Salt separation performance and ion selectivity of the IC-PANF membrane. (A) Performance comparison of the IC-PANF membrane with other state of the art membranes for separating Na_2SO_4. The red star represents the as-prepared IC-PANF membrane (Table S7); (B) The separation performance of IC-PANF membrane for various salts; (C) The water permeance, Na_2SO_4 rejection and the co-ion Cl^-/SO_4^{2-} selectivity of IC-PANF membrane with varying feed concentrations. Error bars represent the standard deviations of three independent measurements.

Supplementary Materials

Materials and Methods

Supplementary Text

Fig. S1 to S50

Tables S1 to S10

References *40-60*